crystals

MDPI

Article

Crystal Growth by the Floating Zone Method of Ce-Substituted Crystals of the Topological Kondo Insulator SmB_6

Monica Ciomaga Hatnean *, Talha Ahmad, Marc Walker and Martin R. Lees and Geetha Balakrishnan

Department of Physics, University of Warwick, Coventry CV4 7AL, UK; S.T.S.Ahmad@warwick.ac.uk (T.A.); M.Walker@warwick.ac.uk (M.W.); m.r.lees@warwick.ac.uk (M.R.L.); G.Balakrishnan@warwick.ac.uk (G.B.)

* Correspondence: M.Ciomaga-Hatnean@warwick.ac.uk

Received: 19 August 2020; Accepted: 14 September 2020 ; Published: 17 September 2020

Abstract: SmB_6 is a mixed valence topological Kondo insulator. To investigate the effect of substituting Sm with magnetic Ce ions on the physical properties of samarium hexaboride, Ce-substituted SmB_6 crystals were grown by the floating zone method for the first time as large, good quality single crystal boules. The crystal growth conditions are reported. Structural, magnetic and transport properties of single crystals of $Sm_{1-x}Ce_xB_6$ ($x = 0.05$, 0.10 and 0.20) were investigated using X-ray diffraction techniques, electrical resistivity and magnetisation measurements. Phase composition analysis of the powder X-ray diffraction data collected on the as-grown boules revealed that the main phase was that of the parent compound, SmB_6. Substitution of Sm ions with magnetic Ce ions does not lead to long-range magnetic ordering in the $Sm_{1-x}Ce_xB_6$ crystals. The substitution with 5% Ce and above suppresses the cross-over from bulk conductivity at high temperatures to surface-only conductivity at low temperatures.

Keywords: crystal growth; optical floating zone method; SmB_6; $Sm_{1-x}Ce_xB_6$; topological insulator; kondo insulator

1. Introduction

Extensive investigations of the physical properties and excitations in the rare earth (RE) hexaboride compounds, REB_6, have been carried out over the past decades. These strongly correlated electron systems display an array of interesting magnetic and electrical properties, such as superconductivity (YB_6 [1–3]), intricate antiferromagnetic ordered phases owing to the displacement of rare earth ions within the rigid framework formed by the boron ions (GdB_6 [4–6]), complex antiferromagnetic phases with Kondo-like characteristics (CeB_6 [7–10]), semimetallic behaviour correlated with the transition to an unusual ferromagnetic state (EuB_6 [11–13]), typical metallic behaviour (LaB_6 [14–16]) or an exotic Kondo-like topological insulating state (SmB_6 [17–19]). Amongst the rare earth hexaboride compounds, cerium and samarium hexaborides have puzzled experimentalists and theoreticians alike, for a long time, in view of their intriguing physical properties. SmB_6 and CeB_6 are isostructural, crystallising in the same cubic CsCl-type structure ($Pm\bar{3}m$ space group) [20–22]. Sm and Ce ions replace the Cs ion, whilst the B_6 cubo-octohedral clusters take the place of the Cl ions at the corners of the cube. Nevertheless, the similarities between samarium and cerium hexaborides stop at the structural level, as they display very unusual, but different physical properties.

SmB_6 has long been known to be a Kondo insulator [23,24]; in recent times, new theoretical and experimental studies demonstrated that samarium hexaboride is a topological Kondo insulator (TKI) exhibiting topological surface properties [18,25–31], although this remains open to further

investigation [32]. SmB_6 is one of the most investigated Kondo insulators, mainly due to its exciting low temperature transport behaviour. As the temperatures decreases, an energy gap arises due to the interaction of the strongly correlated f-electrons and the conducting d-electrons, leading to an exponential increase in the electrical resistance of SmB_6 [33–35]. Unexpectedly, upon further cooling, the resistance of SmB_6 does not continue rising, as would be the case for a conventional insulator, but instead the resistance saturates at a finite value, below 5 K. This plateau in the resistivity has been attributed to a transition from a bulk conductivity characteristic of the high temperature region to a surface-dominated conductivity with bulk insulation at low temperature [36]. SmB_6 is a mixed valence system that does not order magnetically, despite exhibiting antiferromagnetic correlations [33,37–40]. The Sm^{3+}:Sm^{2+} ratio was determined to be independent of the temperature, and equal to approximately 0.6∼0.7:0.4∼0.3 [37,41]. Nevertheless, recent studies have shown that, upon the application of an external pressure, the Sm^{3+} configuration can be stabilised for sufficient time to allow long-range magnetic ordering of the samarium ions [42,43].

CeB_6 is known to have a typical dense Kondo compound behaviour and a complex magnetic phase diagram [44–47]. Cerium hexaboride exhibits Kondo-like behaviour and has a Kondo temperature of $T_K = 19$ K. Upon cooling, CeB_6 undergoes two magnetic ordering transitions: the first to a state in which antiferroquadrupolar and field-induced octupolar order coexist, below $T_Q = 3.2$ K, and then to an antiferromagnetic ordering of the Ce dipoles, below $T_N = 2.3$ K. Moreover, a subsequent study reported a new transition, of unknown origin, at $T_2 = 1.6$ K [45].

Recent progress, e.g., the discovery of the coexistence of an unusual metallic surface state and an insulating bulk state in SmB_6 [19,48] and the observation of the long-range-ordered multipolar phases in CeB_6 [47], has generated new interest in these materials. One route towards the investigation of the exotic metallic surface state arising in SmB_6 and understanding of its topological nature, is through chemical substitution in this TKI with other rare earth ions. Recently, studies have been carried out on Eu, Gd, La, Y and Yb-substituted SmB_6 [18,21,49–54]. High levels of substitution of non-magnetic ions (above 30%), and substitutions with small amounts of magnetic ions, were found to destroy the saturation seen in the low temperature resistivity of pure SmB_6. It would therefore be interesting to investigate the effect that the substitution with a magnetic rare earth, such as Ce, in samarium hexaboride has on the robustness of the topological surface state of this TKI. Such an investigation is of course best carried out on high quality single crystals. In the present work, we investigated single crystals of $Sm_{1-x}Ce_xB_6$, with a focus on studying the effects that the substitution of the magnetic Ce ion have on the structural and physical properties of SmB_6. The physical properties of Ce-substituted SmB_6 samples have previously been investigated; however, this has only been done on polycrystalline samples and flux grown crystals [21,49,54]. Crystals of pure cerium and samarium hexaboride have previously been grown using the floating zone (FZ) technique [55–57]; however, Ce-substituted SmB_6 compounds have only been grown in crystal form using the flux method [54]. SmB_6 crystals grown using Al flux could suffer from contamination by the flux affecting some of the physical properties of the crystals, thereby making it difficult to study the intrinsic properties of pure samarium hexaboride [58]. We have successfully grown, for the first time, crystal boules of $Sm_{1-x}Ce_xB_6$ by the FZ method, which yields large, good quality crystals, free from flux or crucible contamination. The crystals obtained are especially suitable for the investigation of how the substitution with magnetic ions affects the surface and bulk behaviour of this interesting TKI.

2. Materials and Methods

Crystal boules of $Sm_{1-x}Ce_xB_6$ ($x = 0.05$, 0.10 and 0.20) were grown by the floating zone technique [57] using a CSI FZ-T-12000-X_VI-VP four-mirror xenon arc lamp (3 kW) optical image furnace (Crystal Systems Incorporated, Yamanashi, Japan). The crystal quality was checked using a backscattering X-ray Photonic-Science Laue camera system (Photonic-Science, St Leonards-on-Sea, UK). Single crystal samples were aligned for selected experiments, and rectangular prism-shaped

samples with [001], [1-10] and [110] directions perpendicular to the faces of the prism were cut from the $Sm_{1-x}Ce_xB_6$ crystal boules.

Phase composition analysis was carried out using a Panalytical X-Pert Pro MPD diffractometer (Malvern Panalytical Ltd, Malvern, UK) with Cu Kα_1 radiation ($\lambda_{K\alpha 1} = 1.5406$ Å). The diffraction patterns were collected at room temperature over an angular range of 10 to 110° in 2θ with a step size in the scattering angle 2θ of 0.013° and at various scanning times. The analysis of the X-ray patterns was performed using the Fullprof software suite [59].

Chemical composition of the crystal boules was investigated by energy dispersive X-ray spectroscopy (EDX) using a Zeiss SUPRA 55-VP scanning electron microscope (Carl Zeiss GmbH, Jena, Germany). LaB_6 was used as a standard for the EDX measurements. X-ray photoelectron spectroscopy (XPS) analysis was also carried out in order to determine the elemental composition and the valence of the Sm ions. The samples were attached to electrically-conductive carbon tape, mounted on to a sample bar and loaded into a Kratos Axis Ultra DLD (Kratos Analytical Ltd, Manchester, UK) spectrometer (base vacuum of $\sim 2 \times 10^{-10}$ mbar). The measurements were performed using a monochromated Al Kα X-ray source, at room temperature and at a take-off angle of 90° with respect to the surface parallel. The data were analysed in the CasaXPS package (Casa Software Ltd, Teignmouth, UK), using Shirley backgrounds and mixed Gaussian-Lorentzian (Voigt) line-shapes and asymmetry parameters, where appropriate.

Magnetic susceptibility measurements were performed with a Quantum Design Magnetic Property Measurement System (Quantum Design Incorporated, San Diego, USA) on rectangular-prism-shaped $Sm_{1-x}Ce_xB_6$ samples with an applied field parallel to the [100] (tetragonal), [110] (rhombic) and [111] (trigonal) crystallographic directions. The samples were cooled to 1.8 K in zero field and then the susceptibility as a function of temperature up to 300 K was measured on warming and then cooling with an applied field of $H = 500$ Oe.

Alternating current (*ac*) resistivity measurements were performed using a Quantum Design Physical Property Measurement System on bar shaped samples of the $Sm_{1-x}Ce_xB_6$ single crystals using the standard four-probe technique. Silver wire contacts were attached with silver paint, in a linear configuration, to the surfaces of the samples. The resistivity measurements were made from 2 to 300 K on both cooling and warming in zero applied field with an ac current of 1 mA at a frequency of 113 Hz.

3. Results and Discussion

3.1. Crystal Growth

Stoichiometric ratios of high purity SmB_6 (99.9%, American Elements UK, Manchester, UK) and CeB_6 (99.5%, Cerac Incorporated, Milwaukee, USA) powders were mixed together by ball milling for over 15 h, to prepare 5%, 10% and 20% Ce-substituted SmB_6 polycrystalline samples. The resulting materials were then isostatically pressed into rods (typically 5–7 mm diameter and 40–50 mm long) and sintered in an alumina boat, at 1450 °C in a flow of argon gas for 12 h. Before the sintering process, the furnace was evacuated to give a vacuum of $\sim 10^{-5}$ mbar. The resulting polycrystalline feed rods were used for the crystal growth. A binder (polyvinyl alcohol or polyvinyl butyral) was mixed with the powders in some cases to facilitate the formation of the rods.

Crystals of $Sm_{1-x}Ce_xB_6$ ($x = 0.05$, 0.10 and 0.20) were successfully grown by the floating zone method. The growths were carried out in an argon atmosphere at a pressure of ~3 bar, using a growth rate of 18 mm/h. The feed and the seed rods were counter-rotated at ~15–25 rpm. Initially, a crystal boule of SmB_6 was used as a seed. Once good quality crystals were obtained, $Sm_{1-x}Ce_xB_6$ crystal seeds were used for subsequent growths. A dark grey coloured deposition on the quartz tube surrounding the feed and seed rods was observed for all the growths, indicating the evaporation of boron during the growth process.

The $Sm_{1-x}Ce_xB_6$ boules were typically 4–5 mm in diameter and measured approximately 45–50 mm in length. All the crystals obtained developed facets as they grew and two very strong facets were present on almost the entire lengths of most of the grown crystals. Figures 1a–c show photographs of $Sm_{1-x}Ce_xB_6$ crystals grown in argon atmosphere at a growth speed of 18 mm/h. The quality of the grown boules was investigated by X-ray Laue diffraction, and Laue photographs were taken along the length of the boule, on the faceted sides (see Figure 1). The Laue patterns were identical along the whole length of the crystal boules.

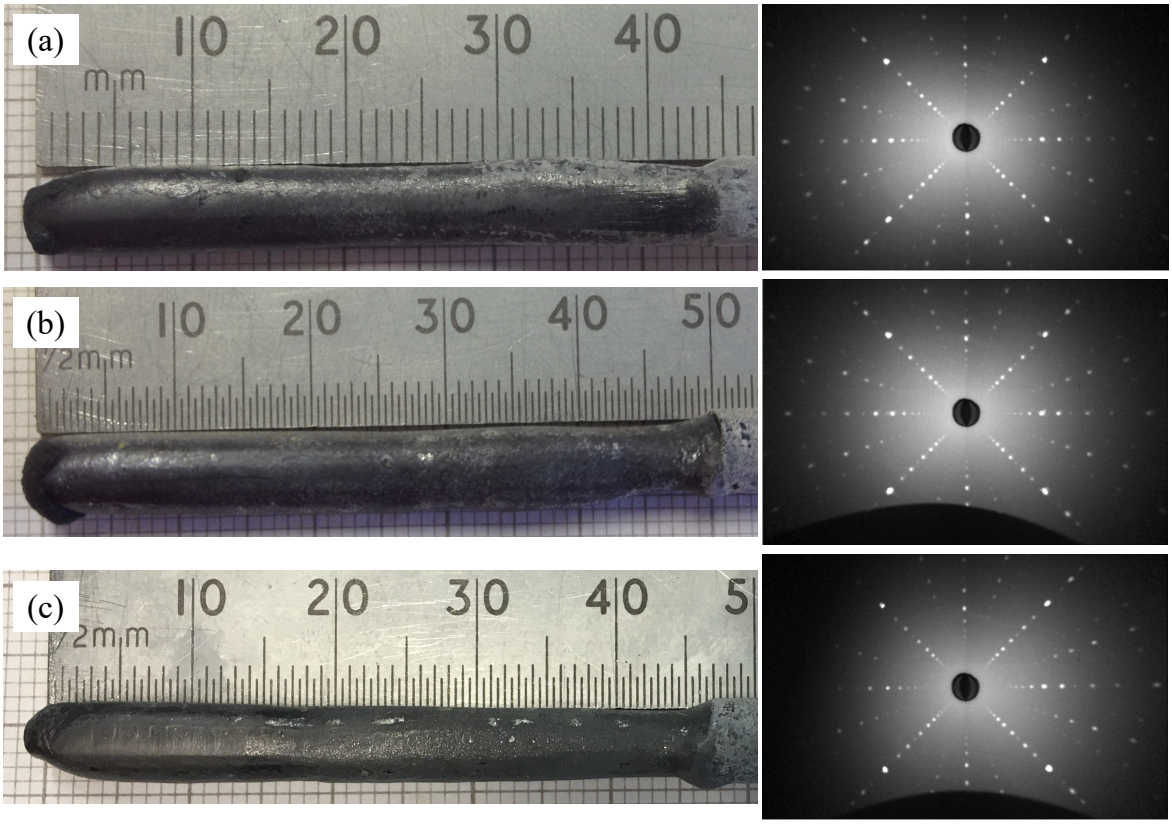

Figure 1. Crystal boules of (**a**) $Sm_{0.95}Ce_{0.05}B_6$, (**b**) $Sm_{0.90}Ce_{0.10}B_6$ and (**c**) $Sm_{0.80}Ce_{0.20}B_6$, prepared by the floating-zone method in argon atmosphere at a growth rate of 18 mm/h. X-ray Laue back reflection photographs show the [001] orientation of aligned $Sm_{1-x}Ce_xB_6$ samples used for the physical properties measurements.

3.2. Structural and Composition Analysis

Structural and phase purity analysis was carried out using powder X-ray diffraction measurements on small pieces of the $Sm_{1-x}Ce_xB_6$ crystals selected from close to the end of each crystal boule. Figures 2a–c show the patterns for $x = 0.05$, 0.10 and 0.20, and profile matching (goodness of fit, GOF = 1.35, 1.51 and 1.92, respectively) to the cubic $Pm\bar{3}m$ space group [20] indicates that in each case the main phase is $Sm_{1-x}Ce_xB_6$, with no significant impurity phases present. One peak that does not belong to the $Pm\bar{3}m$ cubic structure can be observed at ~26.6° in the powder X-ray profiles of each of the $Sm_{1-x}Ce_xB_6$ crystals grown. The impurity was identified to be a hexagonal ($P6_3/mmc$) $SmBO_3$ phase [60]. Lattice parameters calculated from the profile matching were determined to be 4.1351(2) Å, 4.1384(2) Å and 4.1393(2) Å, respectively, for $Sm_{0.95}Ce_{0.05}B_6$, $Sm_{0.90}Ce_{0.10}B_6$ and $Sm_{0.80}Ce_{0.20}B_6$ (see Table 1). The values are in agreement with those reported in previous studies on $Sm_{1-x}Ce_xB_6$ polycrystalline samples [21].

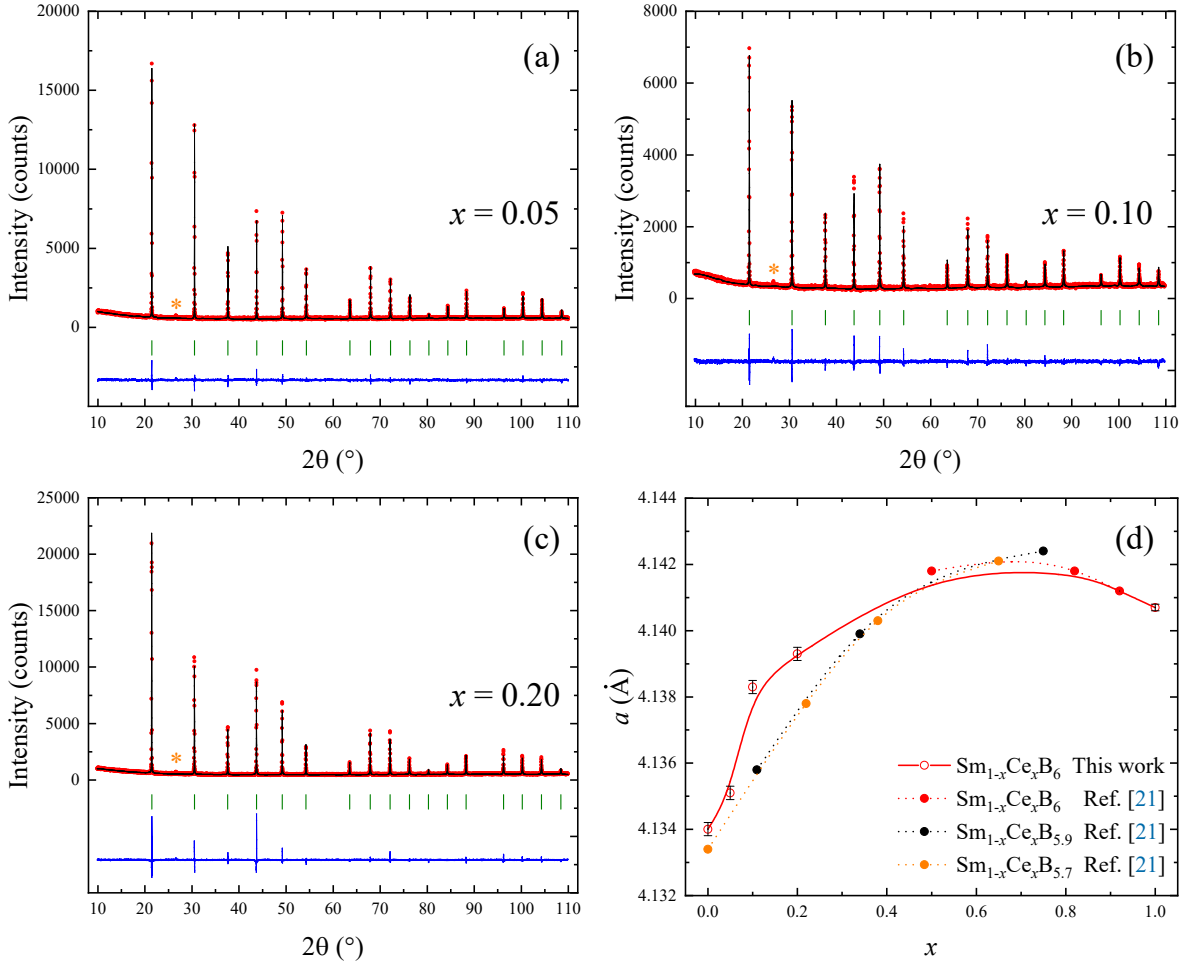

Figure 2. Powder X-ray diffraction patterns of $Sm_{1-x}Ce_xB_6$ with (**a**) $x = 0.05$, (**b**) $x = 0.10$ and (**c**) $x = 0.20$) for samples taken from the crystal boules. The experimental profile (red closed circles) and a full profile matching refinement (black solid line) made using the $Pm\bar{3}m$ cubic structure are shown, with the difference given by the blue solid line. The orange coloured symbols * indicate the impurity peaks belonging to $SmBO_3$ impurity phases. (**d**) Evolution of the lattice parameter, a, as a function of the concentration, x, of the Ce-substituent for $Sm_{1-x}Ce_xB_6$. The experimental values obtained in the present work (red open circles) are also given in Table 1. The previously reported values (red, black and orange closed circles) of the crystallographic parameters for the $Sm_{1-x}Ce_xB_{6-y}$ series [21] are given for completeness.

Figure 2d shows the dependence of the lattice constant on the concentration of Ce for the $Sm_{1-x}Ce_xB_6$ samples. The composition dependence of the cubic parameter, a, does not obey Vegard's law [61], for the $Sm_{1-x}Ce_xB_6$ series. The anomalously large positive deviation observed in Figure 2d can be attributed to the mixed valence of samarium ions [37,38,62]. As the concentration of the Ce-substituent changes from $x = 0$ to 1, the Ce^{3+} ions replace the Sm^{3+} ions preferentially, whereas the concentration of Sm^{2+} ions remains constant [21,38,50]. The effective ionic radius [63,64] of Ce^{3+} (1.01 Å) is larger than the ionic radius of Sm^{3+} (0.958 Å); thus, the substitution of samarium with cerium ions results initially in a lattice expansion (up to $x \sim 0.6$). Further substitution of samarium with cerium is followed by a subtle lattice contraction, which is attributed to the replacement of the larger Sm^{2+} ions (1.15 Å) with Ce^{3+}. A similar effect on the lattice constant has been observed in the case of Gd and La-substituted SmB_6 [38,50,65].

Table 1. Lattice parameters calculated from profile matching the powder X-ray diffraction patterns of the $Sm_{1-x}Ce_xB_6$ (x = 0.05, 0.10 and 0.20) crystals to the $Pm\bar{3}m$ cubic structure. The previously reported structural parameters quoted for other members of the $Sm_{1-x}Ce_xB_{6-y}$ series [21] are included for completeness.

$Sm_{1-x}Ce_xB_{6-y}$	Chemical Composition		a (Å)	Study
	x	y		
SmB_6	0	0	4.1340(2)	Present work
$Sm_{0.95}Ce_{0.05}B_6$	0.05	0	4.1351(2)	Present work
$Sm_{0.90}Ce_{0.10}B_6$	0.10	0	4.1384(2)	Present work
$Sm_{0.89}Ce_{0.11}B_{5.9}$	*0.11*	*0.1*	*4.1358*	*Ref.* [21]
$Sm_{0.80}Ce_{0.20}B_6$	0.20	0	4.1393(2)	Present work
$Sm_{0.78}Ce_{0.22}B_{5.7}$	*0.22*	*0.3*	*4.1378*	*Ref.* [21]
$Sm_{0.66}Ce_{0.34}B_{5.9}$	*0.34*	*0.1*	*4.1399*	*Ref.* [21]
$Sm_{0.62}Ce_{0.38}B_{5.7}$	*0.38*	*0.3*	*4.1403*	*Ref.* [21]
$Sm_{0.50}Ce_{0.50}B_6$	*0.50*	*0*	*4.1418*	*Ref.* [21]
$Sm_{0.35}Ce_{0.65}B_{5.7}$	*0.65*	*0.3*	*4.1421*	*Ref.* [21]
$Sm_{0.25}Ce_{0.75}B_{5.9}$	*0.75*	*0.1*	*4.1424*	*Ref.* [21]
$Sm_{0.18}Ce_{0.82}B_6$	*0.82*	*0*	*4.1418*	*Ref.* [21]
$Sm_{0.08}Ce_{0.92}B_6$	*0.92*	*0*	*4.1412*	*Ref.* [21]
CeB_6	1.00	0	4.1407(1)	Present work

Composition analysis of the crystals of $Sm_{1-x}Ce_xB_6$ was carried out by EDX to determine the concentrations of Ce in each crystal. The results, given in Table 2, show that the ratios for Sm:Ce are similar to the expected chemical compositions for the crystals, relative to the starting compositions of the polycrystalline materials (5%, 10% and 20% Ce-substituted SmB_6 samples).

Table 2. Chemical composition and valence of the Sm ions determined by EDX and XPS for the $Sm_{1-x}Ce_xB_6$ crystal boules grown. The data collected on a pure SmB_6 crystal are included for completeness. The XPS measurements were carried out on a piece of an as-grown SmB_6 crystal boule and on a sample cleaved (in-situ) from the as-grown SmB_6 crystal fragment.

Chemical Composition	Sm:B Ratio (EDX)	Sm:B Ratio (XPS)	Sm Valence Present Work (XPS)	Sm Valence Literature (Refs. [37,41])
SmB_6	1.00(2):5.50(2)	1.00(3):6.4(3)	+2.80(2)	~2.6–2.7
SmB_6 cleaved	-	1:00(3):7.30(3)	+2.72(2)	
$Sm_{1-x}Ce_xB_6$	x (EDX)	x (XPS)	Sm valence (XPS)	
$Sm_{0.95}Ce_{0.05}B_6$	0.07(2)	0.09(3)	+2.86(2)	
$Sm_{0.90}Ce_{0.10}B_6$	0.11(2)	0.14(3)	+2.86(2)	
$Sm_{0.80}Ce_{0.20}B_6$	0.21(2)	0.23(3)	+2.85(2)	

Core level XPS spectra were recorded using a pass energy of 20 eV (resolution ~0.4 eV) on an area of 300 μm × 700 μm of the $Sm_{1-x}Ce_xB_6$ crystals and used to study the electronic states of Sm 4*d*, Ce $3d_{3/2}$ and Ce $3d_{5/2}$ levels, shown in Figure 3. The Sm 4*d* XPS spectrum (see Figure 3a) is composed of one singlet, at 123.5 eV, and one multiplet, at 134.1 eV, separated by approximately 10.6 eV. The Sm^{2+} ($4f^6$ ground-state) feature appears near 129 eV (Sm 4*d* photoelectron line position), which is in agreement with previously published XPS studies on pure SmB_6 [66,67]. The Sm^{3+} ($4f^5$) multiplet appears at a higher binding energy, well separated from the 2+ peak. The contributions of the two features to the XPS spectra were used to determine the valence of the Sm ions. The results, given in Table 2, reveal that $Sm_{1-x}Ce_xB_6$ are mixed valence systems, similar to the parent compound SmB_6 [37,38]. The average Sm valence values of the $Sm_{1-x}Ce_xB_6$ boules are slightly larger than the values determined previously for pure SmB_6 [67–70], due to surface oxidation effects (an increased

concentration of Sm^{3+} to the detriment of the Sm^{2+} ions). Previous XPS results reported an increased average Sm valence and a B/Sm ratio lower than the nominal stoichiometric value of 6:1 when the SmB_6 crystals were exposed to ambient conditions [67]. To confirm this hypothesis, XPS spectra were collected on two SmB_6 crystal samples, an as-grown and a cleaved crystal fragment. The average samarium valence is ~2.8 for the as-grown crystal fragment of SmB_6. In the case of SmB_6 cleaved in-situ from the as-grown crystal, the Sm valence is 2.7, corresponding to a Sm^{3+}:Sm^{2+} ratio of approximately ~0.7:~0.3, which is in agreement with previous results [37,41].

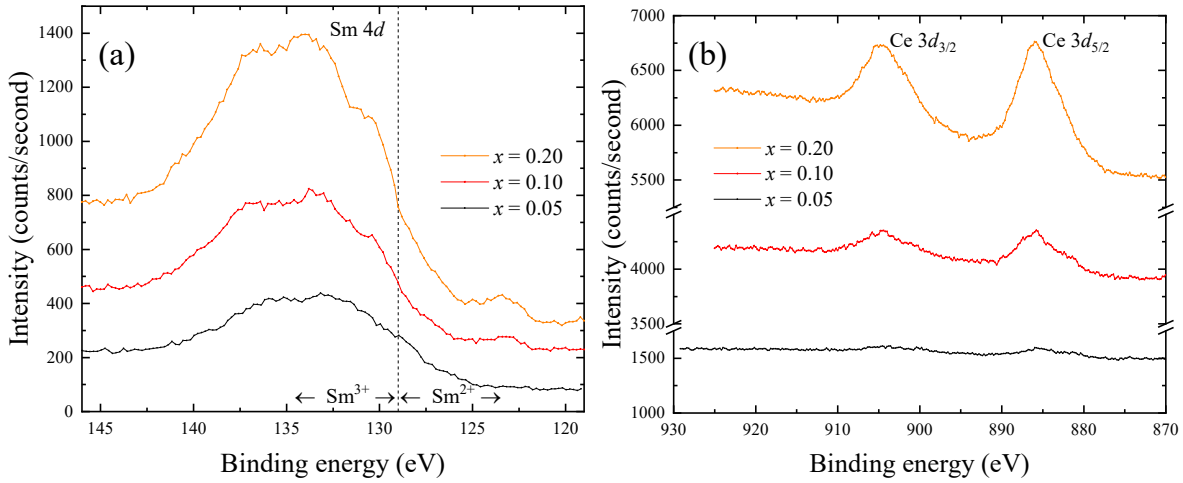

Figure 3. (**a**) Sm 4*d* XPS spectrum and (**b**) Ce $3d_{3/2,5/2}$ XPS spectra collected for the $Sm_{1-x}Ce_xB_6$ (x = 0.05, 0.10, and 0.20) crystal boules.

The Ce 3*d* spectrum, shown in Figure 3b, is comprised of two multiplets, at 885.8 eV and 904.8 eV, corresponding to the spin-orbit split $3d_{5/2}$ and $3d_{3/2}$ core levels. The spin-orbit splitting is approximately 19 eV, with the complex electronic structure of different Ce oxidation states yielding useful spectral features which can be used to distinguish Ce^{3+} and Ce^{4+}. In our data, each component of the Ce 3d XPS spectrum is dominated by two features. The absence of a third component at 916 eV, characteristic of the Ce^{4+} ($4f^0$) [71,72], indicates that the Ce ion is in the 3+ state in the $Sm_{1-x}Ce_xB_6$ samples. The analysis of the XPS results, given in Table 2, allowed us to estimate the amount of Ce-substituent in the $Sm_{1-x}Ce_xB_6$ crystal boules. A comparison of the Ce concentrations determined from the XPS spectra and those estimated from the EDX compositional analysis is provided in Table 2.

3.3. Magnetisation

Zero-field-cooled warming (ZFCW) and field-cooled cooling (FCC) magnetisation versus temperature curves were collected on pieces of the $Sm_{1-x}Ce_xB_6$ (x = 0.05, 0.10 and 0.20) single crystals with an applied field of 500 Oe along three different crystallographic directions ([001], [110] and [111]). The temperature dependence of the *dc* magnetic susceptibility, $\chi(T)$, is shown in Figure 4a. The magnetic susceptibility measured along the different crystallographic directions for all three $Sm_{1-x}Ce_xB_6$ crystals decreased on warming from 1.8 K to room temperature. In addition, for each $Sm_{1-x}Ce_xB_6$ composition, the magnetic susceptibilities collected with field applied along the three different high-symmetry directions all overlap to within experimental error across the whole temperature range.

The temperature dependent magnetic susceptibility of the $Sm_{1-x}Ce_xB_6$ crystals was compared with data collected on a pure SmB_6 crystal grown by the floating zone method [57]. In the temperature range 300 to 60 K, the magnetic susceptibility of Ce-substituted and pure SmB_6 crystals show a similar behaviour, i.e., a gradual increase of $\chi(T)$ with decreasing temperature. Below 60 K, the $Sm_{1-x}Ce_xB_6$ crystals exhibit a more rapid increase in susceptibility, down to 1.8 K. In contrast, the susceptibility data of pure SmB_6 crystals contain a broad maximum centred around 50–60 K, characteristic of a

Kondo insulator, before a more gradual upturn at lower temperatures. Moreover, in the temperature range 1.8–60 K, the magnetic susceptibility of $Sm_{1-x}Ce_xB_6$ crystals increases sharply with increasing Ce content. The change in the magnetic response of both Ce-substituted and pure SmB_6 crystals below 60 K coincides with the increase observed in the resistivity (see Figure 5).

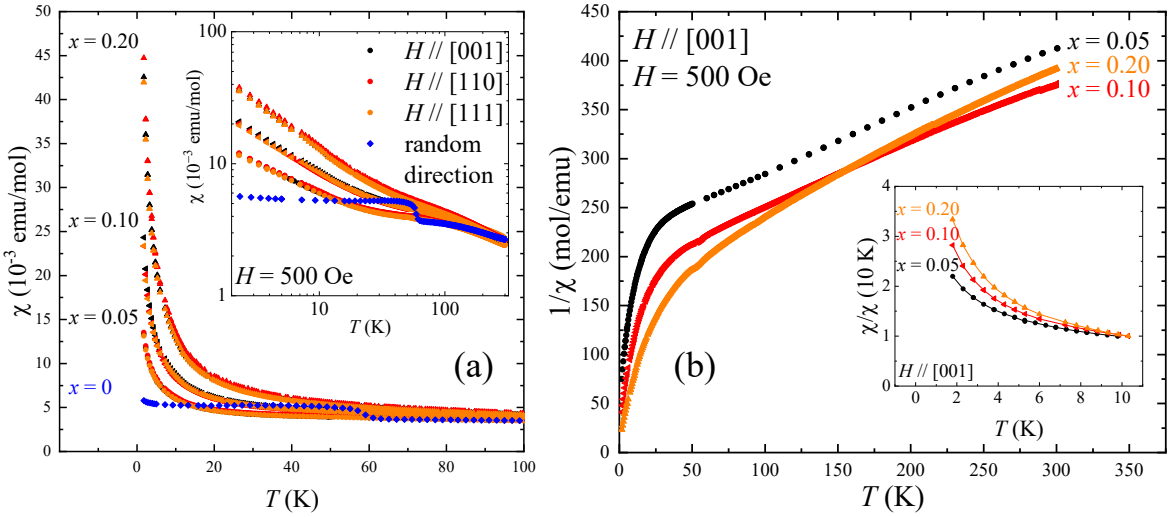

Figure 4. (**a**) Temperature dependence of the *dc* magnetic susceptibility, χ versus T, in the temperature range 1.8–100 K for the $Sm_{1-x}Ce_xB_6$ (x = 0, 0.05, 0.10 and 0.20) crystals, with a magnetic field applied along the [001] (black), [110] (red) and [111] (orange) crystallographic directions. The previously reported susceptibility data for a SmB_6 crystal [57] are given for comparison. The inset shows χ versus T, on a logarithmic scale, in the temperature range 1.8–300 K. (**b**) Temperature dependence of the reciprocal of the *dc* susceptibility, χ^{-1} versus T, of $Sm_{1-x}Ce_xB_6$ for a field applied along the [001] direction. The inset shows the normalised magnetic susceptibilities of $Sm_{1-x}Ce_xB_6$ samples, with a magnetic field applied along the [001] direction. The χ/χ (10 K) versus T data increase rapidly at low temperatures, but with no signature of long-range magnetic order, for all Ce concentrations.

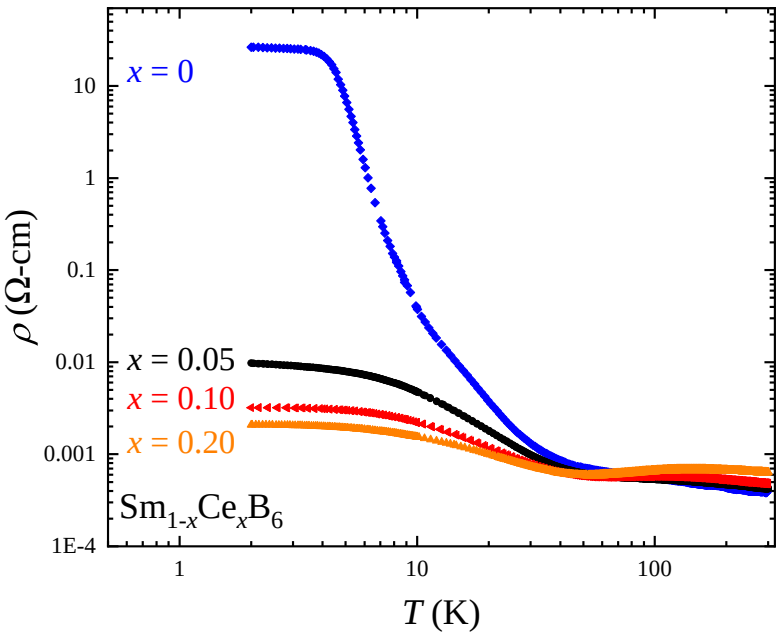

Figure 5. Temperature dependence of the bulk *ac* resistivity, ρ versus T, in the temperature range 1.8–300 K for the $Sm_{1-x}Ce_xB_6$ (x = 0, 0.05, 0.10 and 0.20) crystals. The previously reported resistivity data for a SmB_6 crystal [57] are given for comparison.

Attempts to fit the temperature-dependent reciprocal magnetic susceptibilities, $\chi^{-1}(T)$ (see Figure 4b), in the temperature range 100–300 K reveal that pure SmB_6 and the $Sm_{1-x}Ce_xB_6$ materials all appear to follow a Curie–Weiss law. The effective moment, μ_{eff}, per formula unit at 300 K varies from $2.4(1)\mu_B$ for $x = 0.00$ to $2.5(1)\mu_B$ for $x = 0.20$. The form of $\chi(T)$ for the $Sm_{1-x}Ce_xB_6$ crystals is qualitatively similar than data reported for aluminium flux grown Ce-substituted SmB_6 single crystals, although the effective moments in our samples are substantially lower, especially for lower Ce concentrations [54]. The $\chi(T)$ data are consistent with magnetic response expected for a mixture of $4f^1$ Ce^{3+} ions $\left(2.54\mu_B/Ce^{3+}\right)$ and divalent and trivalent Sm ions in a variety of magnetic and nonmagnetic electronic configurations, $\left(4f^6\right)$, $\left(4f^5d^1\right)$, and $\left(4f^5\right)$ [68,73,74].

A previous study reported that substituting Sm with another magnetic rare earth ion, such as Gd^{3+}, in large concentrations ($\geq$40%), leads to antiferromagnetic ordering at low temperature due to coupling between the Gd sites [18]. This is predicted by the existence of a saturation plateau in the normalised magnetic susceptibility data of 40% Gd-substituted SmB_6. In contrast, the magnetisation curves for our $Sm_{1-x}Ce_xB_6$ crystals exhibit a rapid increase at low temperatures, but with no evidence for the onset of long-range magnetic order down to 2 K, as shown in the inset of Figure 4b. For the Ce^{3+} concentrations used in our work, the magnetic data suggest that the Ce ions are distributed randomly in the lattice.

3.4. Resistivity

Alternating current resistivity versus temperature, $\rho(T)$, measurements were made on bar shaped samples cut from the $Sm_{1-x}Ce_xB_6$ ($x = 0.05$, 0.10 and 0.20) single crystals. The *ac* resistivity data are shown in Figure 5 for temperatures between 1.8 and 300 K. These resistivity data are compared with data for a pure SmB_6 crystal grown by the FZ method and reported in our previous work [57]. At 300 K, the $Sm_{1-x}Ce_xB_6$ samples all have resistivity values similar to SmB_6 and ρ (300 K) increases with x. Below 300 K, SmB_6 exhibits a continuous increase in the bulk electrical resistivity. In contrast, the $\rho(T)$ data for the Ce-substituted samples exhibit a broad maximum centred around 150 K, followed by an increasingly prominent minimum at ~50 K. On further cooling below 50 K, the resistivity of SmB_6 increases by four orders of magnitude, whereas the resistivity of the Ce-substituted samples increases by only a single order of magnitude or less. Nevertheless, the $Sm_{1-x}Ce_xB_6$ samples still have resistivities larger than pure CeB_6, over the entire temperature range studied. The resistivity of CeB_6 is approximately 10^{-5} Ω-cm from 2 to 300 K [75], whereas for the $Sm_{1-x}Ce_xB_6$ samples it is 10^{-3} Ω-cm or higher over the same temperature range, for the $x = 0.20$ sample.

In contrast to the saturation plateau seen in the resistivity of SmB_6 at lowest temperatures, $\rho(T)$ for the $Sm_{1-x}Ce_xB_6$ samples increases monotonically with decreasing temperature below 10 K. These results are in agreement with the transport measurements performed on aluminium flux grown Ce-substituted SmB_6 single crystals [54]. There is an evolution from the TKI behaviour of pure SmB_6 to a dense Kondo system with low temperature spin ordering of CeB_6 [7,8,75]. The data suggest that it is bulk conductivity, modified by crystalline electric field and Kondo effects alongside phonon scattering, that determines the form of the $\rho(T)$ curves for these $Sm_{1-x}Ce_xB_6$ samples over the entire temperature range studied. A more quantitative description of the transport properties of the $Sm_{1-x}Ce_xB_6$ crystals, including extensive measurements in a magnetic field, will be presented elsewhere [76].

4. Conclusions

Crystal boules of $Sm_{1-x}Ce_xB_6$ (x = 0.05, 0.10, and 0.20) compounds were grown, for the first time, by the FZ technique. Investigation of the crystals using X-ray diffraction techniques revealed that the Ce-substituent is successfully incorporated in the SmB_6 structure and that the structural distortions due to the substitution of Sm with Ce follow a similar trend to the one reported for polycrystalline samples of Ce-substituted SmB_6. EDX and XPS results confirm that the Ce concentration is close to the nominal stoichiometric values of $x = 0.05$, 0.10 and 0.20. Analysis of the average Sm valence data determined by XPS on $Sm_{1-x}Ce_xB_6$ and pure SmB_6 samples showed that the results are extremely

dependent on the quality of the surface studied; i.e., an increase in the Sm valence is observed when the surface is exposed to ambient conditions. Magnetic property measurements show that our $Sm_{1-x}Ce_xB_6$ crystals exhibit no sign of long-range magnetic ordering, at substitution concentrations below 20%. Temperature dependent resistivity measurements revealed that a 5% (and above) substitution with Ce suppresses the crossover from bulk to surface conductivity seen in pure SmB_6 as the temperature is reduced. Detailed low temperature magneto-transport measurements are now being carried out to investigate the bulk and surface properties of the $Sm_{1-x}Ce_xB_6$ crystals.

Author Contributions: M.C.H. and T.A. performed the crystal growths; characterisation measurements were carried out by M.C.H. and T.A. with M.W. and M.R.L.; M.C.H., T.A., M.W., M.R.L. and G.B. analysed the data; M.C.H. and T.A. drafted the paper; M.R.L. and G.B. reviewed the manuscript; G.B. secured the funding and managed the project. All authors have read and agreed to the published version of the manuscript.

Funding: Financial support was provided by EPSRC, UK, through grant EP/T005963/1.

Acknowledgments: The authors thank S. York for the EDX compositional analysis, and A. Julian and T. E. Orton for valuable technical support.

Conflicts of Interest: The authors declare no conflict of interest.

Abbreviations

The following abbreviations are used in this manuscript:

RE	Rare earth
TKI	Topological Kondo insulator
FZ	Floating zone
EDX	Energy dispersive X-ray spectroscopy
XPS	X-ray photoelectron spectroscopy
ac	Alternating current
ZFCW	Zero-field-cooled warming
FCC	Field-cooled cooling

References

1. Matthias, B.T.; Geballe, T.H.; Andres, K.; Corenzwit, E.; Hull, G.W.; Maita, J.P. Superconductivity and Antiferromagnetism in Boron-Rich Lattices. *Science* **1968**, *159*, 530. [CrossRef]
2. Lortz, R.; Wang, Y.; Tutsch, U.; Abe, S.; Meingast, C.; Popovich, P.; Knafo, W.; Shitsevalova, N.; Paderno, Y.B.; Junod, A. Superconductivity mediated by a soft phonon mode: Specific heat, resistivity, thermal expansion, and magnetization of YB_6. *Phys. Rev. B* **2006**, *73*, 024512. [CrossRef]
3. Flachbart, K.; Gabáni, S.; Kačmarčik, J.; Mori, T.; Otani, S.; Pavlík, V. Low Temperature Properties and Superconductivity of YB_6 and YB_4. *AIP Conf. Proc.* **2006**, *850*, 635.
4. Coles, B.R.; Griffiths, D. Antiferromagnetic behaviour of GdB_6. *Proc. Phys. Soc. (1958–1967)* **1961**, *77*, 213–215. [CrossRef]
5. Nozaki, H.; Tanaka, T.; Ishizawa, Y. Magnetic behaviour and structure change of GdB_6 single crystals at low temperatures. *J. Phys. C Solid State Phys.* **1980**, *13*, 2751. [CrossRef]
6. Semeno, A.V.; Gil'manov, M.I.; Sluchanko, N.E.; Shitsevalova, N.Y.; Filipov, V.B.; Demishev, S.V. Antiferromagnetic Resonance in GdB_6. *JETP Lett.* **2018**, *108*, 237–242. [CrossRef]
7. Fujita, T.; Suzuki, M.; Komatsubara, T.; Kunii, S.; Kasuya, T.; Ohtsuka, T. Anomalous specific heat of CeB_6. *Solid State Commun.* **1980**, *35*, 569–572. [CrossRef]
8. Takase, A.; Kojima, K.; Komatsubara, T.; Kasuya, T. Electrical resistivity and magnetoresistance of CeB_6 single crystal. *Solid State Commun.* **1980**, *36*, 461–464. [CrossRef]
9. Friemel, G.; Li, Y.; Dukhnenko, A.; Shitsevalova, N.Y.; Sluchanko, N.E.; Ivanov, A.; Filipov, V.B.; Keimer, B.; Inosov, D.S. Resonant magnetic exciton mode in the heavy-fermion antiferromagnet CeB_6. *Nat. Commun.* **2012**, *3*, 830. [CrossRef]
10. Koitzsch, A.; Heming, N.; Knupfer, M.; Büchner, B.; Portnichenko, P.Y.; Dukhnenko, A.V.; Shitsevalova, N.Y.; Filipov, V.B.; Lev, L.L.; Strocov, V.N.; et al. Nesting-driven multipolar order in CeB_6 from photoemission tomography. *Nat. Commun.* **2016**, *7*, 10876. [CrossRef]

11. Guy, C.N.; von Molnar, S.; Etourneau, J.; Fisk, Z. Charge transport and pressure dependence of T_c of single crystal, ferromagnetic EuB_6. *Solid State Commun.* **1980**, *33*, 1055–1058. [CrossRef]
12. Goodrich, R.G.; Harrison, N.; Vuillemin, J.J.; Teklu, A.; Hall, D.W.; Fisk, Z.; Young, D.; Sarrao, J. Fermi surface of ferromagnetic EuB_6. *Phys. Rev. B* **1998**, *58*, 14896–14902. [CrossRef]
13. Nie, S.; Sun, Y.; Prinz, F.B.; Wang, Z.; Weng, H.; Fang, Z.; Dai, X. Magnetic semimetals and quantized anomalous Hall effect in EuB_6. *Phys. Rev. Lett.* **2020**, *124*, 076403. [CrossRef] [PubMed]
14. Arko, A.J.; Crabtree, G.; Karim, D.; Mueller, F.M.; Windmiller, L.R.; Ketterson, J.B.; Fisk, Z. de Haas-van Alphen effect and the Fermi surface of LaB_6. *Phys. Rev. B* **1977**, *13*, 5240–5247. [CrossRef]
15. Bai, L.; Ma, N.; Liu, F. Structure and chemical bond characteristics of LaB_6. *Phys. B Condens. Matter* **2009**, *404*, 4086–4089. [CrossRef]
16. Kasai, H.; Nishibori, E. Spatial distribution of electrons near the Fermi level in the metallic LaB_6 through accurate X-ray charge density study. *Sci. Rep.* **2017**, *7*, 41375. [CrossRef] [PubMed]
17. Wolgast, S.; Kurdak, Ç.; Sun, K.; Allen, J.W.; Kim, D.J.; Fisk, Z. Low-temperature surface conduction in the Kondo insulator SmB_6. *Phys. Rev. B* **2013**, *88*, 180405(R). [CrossRef]
18. Kim, D.J.; Xia, J.; Fisk, Z. Topological surface state in the Kondo insulator samarium hexaboride. *Nat. Mater.* **2014**, *13*, 466–470. [CrossRef]
19. Tan, B.S.; Hsu, Y.T.; Zeng, B.; Ciomaga Hatnean, M.; Harrison, N.; Zhu, Z.; Hartstein, M.; Kiourlappou, M.; Srivastava, A.; Johannes, M.D.; et al. Unconventional Fermi surface in an insulating state. *Science* **2015**, *349*, 287–290. [CrossRef] [PubMed]
20. Stackelberg, M.; Neumann, F. Die kristallstruktur der boride der zusammensetzung MeB_6. *Zeitschrift für Physikalische Chemie* **1932**, *B19*, 314.
21. Aivazov, M.I.; Aleksandrovich, S.V.; Mkrtchyan, V.S. Magnetic susceptibility of $Ce_xLa_{1-x}B_6$, $Ce_xEu_{1-x}B_6$, $Sm_xLa_{1-x}B_6$, and $Sm_xCe_{1-x}B_6$ solid solutions. *Phys. Status Solidi* **1980**, *62*, 109–114. [CrossRef]
22. Funahashi, S.; Tanaka, K.; Iga, F. X-ray atomic orbital analysis of 4f and 5d electron configuration of SmB6 at 100, 165, 230 and 298 K. *Acta Crystallogr. Sect. B Struct. Sci.* **2010**, *66*, 292–306. [CrossRef] [PubMed]
23. Aeppli, G.; Fisk, Z. Kondo insulators. *Comments Condens. Matter Phys.* **1992**, *16*, 155–165.
24. Riseborough, P.S. Heavy fermion semiconductors. *Adv. Phys.* **2000**, *49*, 257–320. [CrossRef]
25. Fu, L.; Kane, C.L.; Mele, E.J. Topological insulators in three dimensions. *Phys. Rev. Lett.* **2007**, *98*, 106803. [CrossRef] [PubMed]
26. Moore, J.E.; Balents, L. Topological invariants of time-reversal-invariant band structures. *Phys. Rev. B* **2007**, *75*, 121306(R). [CrossRef]
27. Roy, R. Topological phases and the quantum spin Hall effect in three dimensions. *Phys. Rev. B* **2009**, *79*, 195322. [CrossRef]
28. Dzero, M.; Sun, K.; Galitski, V.; Coleman, P. Topological Kondo insulators. *Phys. Rev. Lett.* **2010**, *104*, 106408. [CrossRef]
29. Takimoto, T. SmB_6: A promising candidate for a topological insulator. *J. Phys. Soc. Jpn.* **2011**, *80*, 123710. [CrossRef]
30. Dzero, M.; Sun, K.; Coleman, P.; Galitski, V. Theory of topological Kondo insulators. *Phys. Rev. B* **2012**, *85*, 045130. [CrossRef]
31. Neupane, M.; Alidoust, N.; Xu, S.Y.; Kondo, T.; Ishida, Y.; Kim, D.J.; Liu, C.; Belopolski, I.; Jo, Y.J.; Chang, T.R.; et al. Surface electronic structure of the topological Kondo-insulator candidate correlated electron system SmB_6. *Nat. Commun.* **2013**, *4*, 2991. [CrossRef] [PubMed]
32. Hlawenka, P.; Siemensmeyer, K.; Weschke, E.; Varykhalov, A.; Sánchez-Barriga, J.; Shitsevalova, N.Y.; Dukhnenko, A.V.; Filipov, V.B.; Gabáni, S.; Flachbart, K.; et al. Samarium hexaboride is a trivial surface conductor. *Nat. Commun.* **2018**, *9*, 517. [CrossRef] [PubMed]
33. Menth, A.; Buehler, E.; Geballe, T.H. Magnetic and semiconducting properties of SmB_6. *Phys. Rev. Lett.* **1969**, *22*, 295–297. [CrossRef]
34. Allen, J.W.; Batlogg, B.; Wachter, P. Large low-temperature Hall effect and resistivity in mixed-valent SmB_6. *Phys. Rev. B* **1979**, *20*, 4807–4813. [CrossRef]
35. Cooley, J.C.; Aronson, M.C.; Fisk, Z.; Canfield, P.C. SmB_6: Kondo insulator or exotic metal? *Phys. Rev. Lett.* **1995**, *74*, 1629–1632. [CrossRef] [PubMed]

36. Phelan, W.; Koohpayeh, S.; Cottingham, P.; Freeland, J.; Leiner, J.; Broholm, C.; McQueen, T. Correlation between bulk thermodynamic measurements and the low-temperature-resistance plateau in SmB_6. *Phys. Rev. X* **2014**, *4*, 031012.
37. Kasuya, T.; Takegahara, K.; Fujita, T.; Tanaka, T.; Bannai, E. Valence fluctuating state in SmB_6. *J. Phys. Colloq.* **1979**, *40*, 308–313. [CrossRef]
38. Kasuya, T. Mixed-salence state in SmB_6. *Europhys. Lett. (EPL)* **1994**, *26*, 283–287. [CrossRef]
39. Flachbart, K.; Gabáni, S.; Herrmannsdörfer, T.; Konovalova, E.; Paderno, Y.; Pavlík, V. Low-temperature magnetic properties of SmB_6. *Phys. B Condens. Matter* **2000**, *284–288*, 1353–1354. [CrossRef]
40. Gheidi, S.; Akintola, K.; Akella, K.S.; Côté, A.M.; Dunsiger, S.R.; Broholm, C.; Fuhrman, W.T.; Saha, S.R.; Paglione, J.; Sonier, J.E. Intrinsic Low-Temperature Magnetism in SmB_6. *Phys. Rev. Lett.* **2019**, *123*, 197203. [CrossRef]
41. Chazalviel, J.N.; Campagna, M.; Wertheim, G.K.; Schmidt, P.H.; Longinotti, L.D. Electronic structure of SmB_6 and related rare-earth borides by x-ray photoelectron spectroscopy. *Physica B+C* **1977**, *86–88*, 237–238. [CrossRef]
42. Barla, A.; Derr, J.; Sanchez, J.P.; Salce, B.; Lapertot, G.; Doyle, B.P.; Rüffer, R.; Lengsdorf, R.; Abd-Elmeguid, M.M.; Flouquet, J. High-Pressure Ground State of SmB_6: Electronic Conduction and Long Range Magnetic Order. *Phys. Rev. Lett.* **2005**, *94*, 166401. [CrossRef] [PubMed]
43. Miyazaki, H.; Hajiri, T.; Ito, T.; Kunii, S.; Kimura, S.I. Momentum-dependent hybridization gap and dispersive in-gap state of the Kondo semiconductor SmB_6. *Phys. Rev. B* **2012**, *86*, 075105. [CrossRef]
44. Hall, D.; Fisk, Z.; Goodrich, R.G. Magnetic-field dependence of the paramagnetic to the high-temperature magnetically ordered phase transition in CeB_6. *Phys. Rev. B* **2000**, *62*, 84–86. [CrossRef]
45. Goodrich, R.G.; Young, D.P.; Hall, D.; Balicas, L.; Fisk, Z.; Harrison, N.; Betts, J.; Migliori, A.; Woodward, F.M.; Lynn, J.W. Extension of the temperature-magnetic field phase diagram of CeB_6. *Phys. Rev. B* **2004**, *69*, 054415. [CrossRef]
46. Terzioglu, C.; Ozturk, O.; Kilic, A.; Goodrich, R.; Fisk, Z. Magnetic and electronic measurements in CeB_6. *J. Magn. Magn. Mater.* **2006**, *298*, 33–37. [CrossRef]
47. Portnichenko, P.; Akbari, A.; Nikitin, S.; Cameron, A.; Dukhnenko, A.; Filipov, V.; Shitsevalova, N.; Čermák, P.; Radelytskyi, I.; Schneidewind, A.; et al. Field-Angle-Resolved Magnetic Excitations as a Probe of Hidden-Order Symmetry in CeB_6. *Phys. Rev. X* **2020**, *10*, 021010. [CrossRef]
48. Hartstein, M.; Toews, W.H.; Hsu, Y.T.; Zeng, B.; Chen, X.; Ciomaga Hatnean, M.; Zhang, Q.R.; Nakamura, S.; Padgett, A.S.; Rodway-Gant, G.; et al. Fermi surface in the absence of a Fermi liquid in the Kondo insulator SmB_6. *Nat. Phys.* **2018**, *14*, 166–172. [CrossRef]
49. Aivazov, M.I.; Aleksandrovich, S.V.; Evseev, B. Physical properties of solid solutions $Sm_xCe_{1-x}B_6$. *Inorg. Mater.* **1980**, *16*, 300–303.
50. Kasaya, M.; Tarascon, J.M.; Etourneau, J. Study of the valence transition in La- and Yb-substituted SmB_6. *Solid State Commun.* **1980**, *33*, 1005–1007. [CrossRef]
51. Liu, B.; Kasaya, M.; Iga, F.; Kasuya, T. Kondo effect in $Sm_{1-y}Yb_yB_6$ and $Tm_{1/2}Yb_{1/2}B_6$. *J. Magn. Magn. Mater.* **1985**, *47-48*, 472–474. [CrossRef]
52. Yeo, S.; Song, K.; Hur, N.; Fisk, Z.; Schlottmann, P. Effects of Eu doping on SmB_6 single crystals. *Phys. Rev. B* **2012**, *85*, 115125. [CrossRef]
53. Gabáni, S.; Flachbart, K.; Bednarčík, J.; Welter, E.; Filipov, V.; Shitsevalova, N. Investigation of Mixed Valence State of $Sm_{1-x}B_6$ and $Sm_{1-x}La_xB_6$ by XANES. *Acta Phys. Pol. A* **2014**, *126*, 292–306. [CrossRef]
54. Miao, L.; Min, C.H.; Xu, Y.; Huang, Z.; Kotta, E.C.; Basak, R.; Song, M.S.; Kang, B.Y.; Cho, B.K.; Kißner, K.; et al. Robust surface states and coherence phenomena in magnetically alloyed SmB_6. *arXiv* **2020**, arXiv:1907.07074v2.
55. Otani, S.; Nakagawa, H.; Nishi, Y.; Kieda, N. Floating zone growth and high temperature hardness of rare-earth hexaboride crystals: LaB_6, CeB_6, PrB_6, NdB_6, and SmB_6. *J. Solid State Chem.* **2000**, *154*, 238–241. [CrossRef]
56. Balakrishnan, G.; Lees, M.R.; Paul, D.M. Growth of large single crystals of rare earth hexaborides. *J. Cryst. Growth* **2003**, *256*, 206–209. [CrossRef]
57. Ciomaga Hatnean, M.; Lees, M.R.; Paul, D.M.; Balakrishnan, G. Large, high quality single-crystals of the new Topological Kondo Insulator, SmB_6. *Sci. Rep.* **2013**, *3*, 3071. [CrossRef]

58. Thomas, S.M.; Ding, X.; Ronning, F.; Zapf, V.; Thompson, J.D.; Fisk, Z.; Xia, J.; Rosa, P.F.S. Quantum oscillations in flux-grown SmB_6 with embedded aluminum. *Phys. Rev. Lett.* **2019**, *122*, 166401. [CrossRef]
59. Rodríguez-Carvajal, J. Recent advances in magnetic structure determination by neutron powder diffraction. *Physica B* **1993**, *192*, 55–69. [CrossRef]
60. Newnham, R.E.; Redman, M.J.; Santoro, R.P. Crystal Structure of yttrium and other rare-earth borates. *J. Am. Ceram. Soc.* **1963**, *46*, 253–256. [CrossRef]
61. Vegard, L. Die konstitution der mischkristalle und die raumfüllung der atome. *Z. Phys.* **1921**, *5*, 17–26. [CrossRef]
62. Tarascon, J.; Isikawa, Y.; Chevalier, B.; Etoumeau, J.; Hagenmuller, P.; Kasaya, M. Valence transition of samarium in hexaboride solid solutions $Sm_{1-x}M_xB_6$ (M = Yb^{2+}, Sr^{2+}, La^{3+}, Y^{3+}, Th^{4+}). *J. Phys.* **1980**, *41*, 1135–1140. [CrossRef]
63. Shannon, R.D. Revised effective ionic radii and systematic studies of interatomic distances in halides and chalcogenides. *Acta Crystallogr. Sect. A* **1976**, *32*, 751–767. [CrossRef]
64. Jia, Y.Q. Crystal radii and effective ionic radii of the rare earth ions. *J. Solid State Chem.* **1991**, *95*, 184–187. [CrossRef]
65. Konovalova, E.S.; Paderno, Y.B.; Lundstrem, T.; Finkel'shtein, L.D.; Efremova, N.N.; Dudnik, E.M. Effect of vacancies and foreign metal ions on the valent state of samarium in SmB_6. *Sov. Powder Metall. Met. Ceram.* **1982**, *21*, 820–823. [CrossRef]
66. Chazalviel, J.N.; Campagna, M.; Wertheim, G.K.; Schmidt, P.H. Study of valence mixing in SmB_6 by x-ray photoelectron spectroscopy. *Phys. Rev. B* **1976**, *14*, 4586–4592. [CrossRef]
67. Heming, N.; Treske, U.; Knupfer, M.; Büchner, B.; Inosov, D.S.; Shitsevalova, N.Y.; Filipov, V.B.; Krause, S.; Koitzsch, A. Surface properties of SmB_6 from x-ray photoelectron spectroscopy. *Phys. Rev. B* **2014**, *90*, 195128. [CrossRef]
68. Mizumaki, M.; Tsutsui, S.; Iga, F. Temperature dependence of Sm valence in SmB_6 studied by X-ray absorption spectroscopy. *J. Phys. Conf. Ser.* **2009**, *176*, 012034. [CrossRef]
69. Emi, N.; Mito, T.; Kawamura, N.; Mizumaki, M.; Ishimatsu, N.; Pristáš, G.; Kagayama, T.; Shimizu, K.; Osanai, Y.; Iga, F. Temperature and pressure dependences of Sm valence in intermediate valence compound SmB_6. *Phys. B Condens. Matter* **2018**, *536*, 197–199. [CrossRef]
70. Savchenkov, P.S.; Alekseev, P.A.; Podlesnyak, A.; Kolesnikov, A.I.; Nemkovski, K.S. Intermediate-valence state of the Sm and Eu in SmB_6 and $EuCu_2Si_2$: Neutron spectroscopy data and analysis. *J. Phys. Condens. Matter* **2018**, *30*, 055801. [CrossRef]
71. Paparazzo, E. On the curve-fitting of XPS Ce(3d) spectra of cerium oxides. *Mater. Res. Bull.* **2011**, *46*, 323–326. [CrossRef]
72. Revoy, M.N.; Scott, R.W.J.; Grosvenor, A.P. Ceria nanocubes: Dependence of the electronic structure on synthetic and experimental conditions. *J. Phys. Chem. C* **2013**, *117*, 10095–10105. [CrossRef]
73. Gabáni, S.; Flachbart, K.; Pavlík, V.; Herrmannsdorfer, T.; Konovalova, E.; Paderno, Y.; Briančin, J.; Trpčevská, J. Magnetic properties of $Sm_{1-x}B_6$ and $Sm_{1-x}La_xB_6$ solid solutions. *Czechoslov. J. Phys.* **2002**, *52*, A225–A228. [CrossRef]
74. Nickerson, J.C.; White, R.M.; Lee, K.N.; Bachmann, R.; Geballe, T.H.; Hull, G.W. Physical properties of SmB_6. *Phys. Rev. B* **1971**, *3*, 2030–2042. [CrossRef]
75. Tanaka, T.; Nishitani, R.; Oshima, C.; Bannai, E.; Kawai, S. The preparation and properties of CeB_6, SmB_6, and GdB_6. *J. Appl. Phys.* **1980**, *51*, 3877. [CrossRef]
76. Ciomaga Hatnean, M.; Lees, M.R.; Ahmad, T.; Balakrishnan, G. University of Warwick, Coventry. 2020, in preparation.